# Optimization-Inspired Pin-Fin Array for Supercritical Carbon Dioxide Recuperator

Matthew Searle*[1,2], Sridharan Ramesh[1,2], and Douglas Straub[1]
[1]National Energy Technology Laboratory, 3610 Collins Ferry Road, Morgantown, WV 26505, USA
[2]NETL Support Contractor, 3610 Collins Ferry Road, Morgantown, WV 26505, USA

## Abstract

Additively manufactured heat exchangers are one possible route to cost-effective $sCO_2$ power cycles. In this paper, experimental results are obtained for two helical pin fin tubes that were designed following parametric optimization of the fin array. Neither the numerical optimization nor the experimental testing have been previously reported in the literature. The two tube designs were, (1) the optimization inspired design, and (2) the optimization-inspired design with a fin diameter increased by a factor of 2. To characterize the print, the designs were scanned using X-ray computed tomography to measure feature sizes and heat transfer area. The optimization was conducted in a commercial, computational fluid dynamics code. The code solved the Reynolds Averaged Navier-Stokes (RANS) and energy equations with turbulence closure provided by the shear stress transport (SST) k-$\omega$ model. In the experiments, the Nusselt number augmentation was measured using the Wilson plot technique and the friction factor was determined with mass flow and pressure drop measurements. The experimental testing indicated that the optimization-inspired design had a friction factor that was four times less than the baseline tube design at equal Nusselt number. Additionally, the optimization-inspired design had a 14% improvement in Nusselt number, at equal friction factor, relative to the best performing computational fluid dynamics (CFD) trial points. Tube design (2), with the larger diameter pin fins, had similar performance, within experimental error, as the tube with the smaller diameter pin fins (1). Both tubes achieved overall fin array efficiencies near 1. A performance factor, $V/V_0$, equal to the volume of the enhanced heat exchanger divided by the volume of the baseline (no-fins) heat exchanger, is recommended to quantify internal cooling performance. The experimental shell and tube heat exchanger, using the additively manufactured tube, is competitive with printed circuit heat exchangers in its pressure drop class and could be further improved by optimizing a shell-and-tube heat exchanger utilizing this heat transfer enhancement feature.

## Keywords

*Supercritical carbon dioxide, direct cycle, heat transfer, additive manufacturing, parametric optimization*

## Nomenclature

| | |
|---|---|
| $A$ | area [m$^2$] |
| CFD | computational fluid dynamics |
| CT | computational tomography |

* Corresponding author: matthew.searle@netl.doe.gov
*Preprint for submission to Applied Thermal Engineering*

$D$ tube diameter [m]

$f$ friction factor [-]

HEET Heat Exchange and Experimental Testing

$h$ heat transfer coefficient [W/m$^2$-K]

i specific enthalpy [J/kg]

$k$ thermal conductivity [W/m-K]

$l$ tube length [m]

$L$ fin length [m]

$m$ recuperator mass [kg]

$m_{sp}$ specific recuperator mass, $m_{sp} = m/Q$ [kg/kW]

$\dot{m}$ mass flow rate [kg/s]

$M$ material volume per unit length [m$^3$/m]

$n$ fin equation constant [m$^{-1}$]

$Nu$ Circumferential and pitch averaged Nusselt number, $Nu = hD/k$ [-]

$\overline{Nu}$ Average Nusselt number $\overline{Nu} = \bar{h}D/k$ [-]

$P$ fin perimeter [m]

$Q$ recuperator heat rate, $Q = \dot{m}_c(i_{c,o} - i_{c,i})$ [W]

$Q$" heat flux [W/m$^2$]

$Re$ Reynolds number, $Re = \rho VD/\mu$ [-]

$R$ thermal resistance [K/W]

sCO2 supercritical carbon dioxide

$TPF$ thermal performance factor, $TPF = (Nu/Nu_0)/(f/f_0)^{1/3}$ [-]

$TPF^*$ thermal performance factor, $TPF^* = TPF/(Fin\ Volume/Length)$ [m$^{-2}$]

$TPF_2$ thermal performance factor 2, $TPF_2 = TPF/(Fin\ Volume)$ [m$^{-3}$]

$TPF_3$ thermal performance factor 3, $TPF_3 = TPF/(Total\ Volume/Length)$ [m$^{-2}$]

$TPF_4$ thermal performance factor 4, $TPF_4 = TPF^*$ [m$^{-2}$]

$V$ volume [m$^3$]

$\Delta P$ tube pressure drop [kPa]

$\Delta T_{lm}$ log mean temperature difference. [K]

$\eta$ overall fin array efficiency [-]

$\eta_f$ fin efficiency [-]

$\rho$ density [kg/m$^3$]

$\mu$ viscosity [Pa-s]

Subscripts

$0$ smooth, finless tube

$0c$ cold, calculated

$a$ single, enhanced (rough) tube

$b$ bulk

$c$ cold (tube)

$f$ fluid

$fin$ fin

$i$ inlet

$m$ metal

$ov$ overall

$o$ outlet

$p$ primary, tube wall

$n$ single, smooth tube

$r$ recuperator

$s$ secondary, fin area

$w$ wall

$xs$ fin cross section

# 1. Introduction

Supercritical carbon dioxide ($sCO_2$) Brayton cycles are being considered as a potential replacement for classical steam Rankine power cycles [1]. The $sCO_2$ Brayton cycle has the following advantages over the Rankine cycle: increased efficiency (lower fuel operating costs, reduced $CO_2$ emissions for fossil powered plants), decreased capital cost, smaller plant footprint and lower weight, and faster transient response.

The flexibility of the $sCO_2$ Brayton cycle to function with various primary heat sources (fossil (direct/indirect), solar, nuclear) is an additional benefit.

The U.S. Department of Energy's (DOE) Office of Fossil Energy and Carbon Management has funded internal and extramural research in $sCO_2$ Brayton cycle development, including a 10 MW indirect cycle demonstration plant [2].

A simplified schematic of a recuperated $sCO_2$ Brayton cycle, typical of the above referenced demonstration plant, is displayed in Figure 1. Main components including the main and bypass compressor, high and low temperature recuperators, primary heater, turbine, and pre-cooler are shown.

As shown, recuperated $sCO_2$ Brayton cycles have at least three heat exchangers: heater, cooler, and recuperator (with the recuperator typically divided into a high temperature section and a low temperature section to prevent a pinch point and to reduce the required quantity of high temperature material). The heat duty of the recuperator is at least three times the heater [1]. The cost of the heat exchangers is a significant portion of the cost of the plant. Reducing $sCO_2$ heat exchanger cost and size is recommended to increase market penetration of the $sCO_2$ Brayton cycle [1].

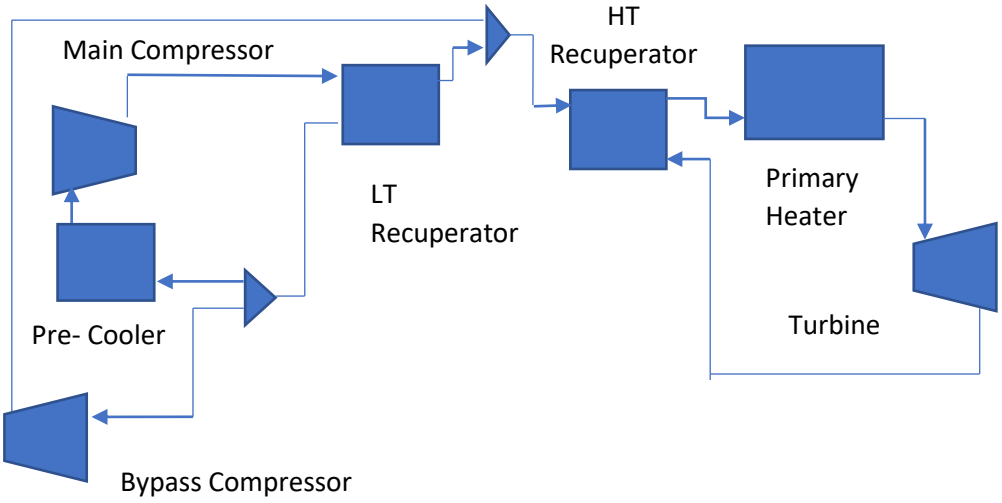


*Figure 1: Simplified schematic of $sCO_2$ Brayton cycle with components labeled.*

The helical pin fin concept was introduced in prior work to create an enhanced heat transfer surface on the interior of an additively manufactured, shell-and-tube heat exchanger [3]. Five tube designs were fabricated and evaluated to establish a baseline. Pins were arranged in a helical pattern to create swirl flow, generate turbulence, and increase heat transfer area.

More recent experiments in the same test facility [4-5] studied the use of heat transfer enhancement features for cooling turbine blades in $sCO_2$ direct-fired power cycles. These studies demonstrated high performance for traditional cooling enhancement features, operating in an $sCO_2$ environment, at Reynolds numbers greater than $1 \times 10^5$. This contrasts with the decreased performance for identical features operating in air at Reynolds numbers greater than $1 \times 10^5$ [3]. Other cooling technologies for turbine blade/vane cooling in these power cycles have been studied and are related to heat transfer

flows in $sCO_2$ cycle heat exchangers. These studies found that heat transfer in impinging $sCO_2$ jets was significantly underpredicted by air-based impingement correlations while air-based pin fin correlations successfully predicted the cooling performance [6-7].

The state-of-the-art technology for $sCO_2$ heat exchangers is the printed circuit heat exchanger [2, 8]. It is utilized due to its strength and reliability at high pressures, acceptable thermal-fluid performance, and mature manufacturing process. While some early studies utilized conventional shell-and-tube heat exchangers to verify heat transfer correlations [9], later studies transitioned to diffusion-bonded, PCHEs [10] to achieve higher effectiveness.

Further innovations in the geometry of PCHEs, such as the stacked-sheet heat exchanger (where cooling passages flow through hole arrays in stacked and bonded sheets) may continue to improve the performance and durability of the technology [11]. Alternatively, thermal-hydraulic performance of PCHEs has been improved by reducing the heat exchanger pressure drop. In one study, novel PCHE flow passages including discrete, staggered rectangular or airfoil-shaped fins were shown to significantly reduce pressure drop [12]. In another approach, the architecture of the heat exchanger was changed to create a matrix of recuperator unit cells which could transfer heat in parallel [13]. Microtube and shell heat exchangers have also been considered [14, 15].

Other investigators have recognized cost-effectiveness challenges with PCHEs which could be resolved through alternate manufacturing technologies. One study proposed using a vacuum assisted brazing technique to assemble a sCO2 recuperator [16]. The design achieved a reduced feature count since the assembly process could accept more complex geometries and utilize inserts. Additional cost benefits relative to PCHEs were less stringent geometric dimensioning and tolerancing (GD&T) for surface finishes, reduced number of bond joints, thermal stresses reduced by utilizing a flexible core, and a 54.7% and 45.2 % reduction in weight and volume, respectively.

Additive manufacturing has been applied to improve the performance of other single-phase heat exchanger technologies but has not been extensively studied for sCO2 applications. One study developed a novel geometry for heat exchange between water (hot fluid) to R245fa (cold fluid) [17, Sabau 2020]. To improve exchanger performance, each fluid pathway transitioned from tube-flow to shell-flow. The advanced designs were compared to a 5 kW off-the-shelf, shell-and-tube heat exchanger. The overall heat transfer coefficient of the advanced designs was 16% to 32% greater than the baseline.

To be economically competitive, the performance of an additively manufactured $sCO_2$ heat exchanger needs to significantly exceed the performance of a-state-of-the art printed circuit heat exchanger or other competing technology. Prior research and development at NETL and Oak Ridge National Laboratory demonstrated an additively-manufactured recuperator with higher heat duty per unit mass than a conventional printed circuit heat exchanger [18].

The novel contribution of the present work is to explore if commercial CFD and optimization codes could be applied to improve the helical patterned pin concept [3] and to explore the effects of additive manufacture on its thermal performance. The present study reports the numerical approach and resulting optimization-inspired design, the experimental test, and a comparison between the experimental results and the CFD prediction.

## 2. Numerical Approach and Optimization Strategy

Steady State Reynolds Averaged Navier-Stokes (RANS) simulations were conducted with the ANSYS Fluent CFD package. The continuity and momentum equations in tensor form are shown in Equations (1) and (2) as documented in the software theory guide [19]. Turbulence modeling was handled using the k-$\omega$ Shear Stress Transport (SST) model since this model showed better agreement with Petukhov's correlation [20].

$$\frac{\partial \rho}{\partial t} + \frac{\partial}{\partial x_i}(\rho u_i) = 0 \tag{1}$$

$$\begin{aligned} &\frac{\partial}{\partial t}(\rho u_i) + \frac{\partial}{\partial x_j}(\rho u_i u_j) \\ &\quad = -\frac{\partial p}{\partial x_i} + \frac{\partial}{\partial x_j}\left[\mu\left(\frac{\partial u_i}{\partial x_j} + \frac{\partial u_j}{\partial x_i} - \frac{2}{3}\delta_{ij}\frac{\partial u_l}{\partial x_l}\right)\right] \\ &\quad + \frac{\partial}{\partial x_j}\left(\mu_t\left(\frac{\partial u_i}{\partial x_j} + \frac{\partial u_j}{\partial x_i}\right)\right. \\ &\quad \left. - \frac{2}{3}\left(\rho k + \frac{\mu_t \partial u_k}{\partial x_k}\right)\delta_{ij}\right) \end{aligned} \tag{2}$$

To obtain physically realistic results, wall $y^+$ varied from 1-2. A coupled, pseudo-transient solver was utilized. Convergence residuals achieved $10^{-6}$ within 200 iterations and a hard limit at 1,000 iterations was applied for each optimization case.

Simulation boundary parameters are displayed in Table 1. For momentum, the inlet was a mass flow rate boundary and the outlet was a pressure boundary. The wall condition was a smooth, no-slip wall which was handled by a boundary layer refined mesh and viscous sublayer boundary conditions, applied automatically by the ANSYS SST k-$\omega$ model for the boundary layer mesh. A schematic of the wall thermal boundary conditions is shown in Figure 2. These consisted of a uniform inlet temperature and uniform wall temperature. Conjugate effects within the pins were not modeled, thus the fin temperature was uniform. This simplified boundary condition was applied to make the optimization computationally tractable. The experimental approach accounted for the fin effectiveness and found that the overall fin effectiveness was 0.97 for both Exp. Tube 1 and Exp. Tube 2, validating the simulation boundary condition assumption.

The working fluid for the simulations was $CO_2$ with uniform properties. Simulations showed that the axial bulk temperature variation was 2-4 K and, thus, property variation in each test would be small. Furthermore, variation in $c_P$ from the wall temperature to the bulk temperature was less than 12%.

*Table 1: CFD parameters and boundary conditions.*

| Parameter | Value |
|---|---|
| Inlet Temperature, $T$ | 400 K |
| Inlet Pressure, $P$ | 15.5 MPa |
| Density, $\rho$ | 279.6 kg/m$^3$ |
| Viscosity, $\mu$ | 2.65 x 10$^{-5}$ Pa-s |
| Specific Heat, $c_p$ | 1.67 kJ/kg-K |
| Thermal Conductivity, $k$ | 0.0392 W/m-K |
| Reynolds Number, $Re$ | 120,306 |
| Prandtl Number, $Pr$ | 1.13 |
| Nusselt Number, $Nu_0$ (Dittus Boelter) | 279.93 |
| Friction Factor, $f_0$ (McAdams) | 0.0177 |
| Inlet Mass Flow Rate | 0.01 kg/s |
| Wall Temperature (uniform) | 425 K |

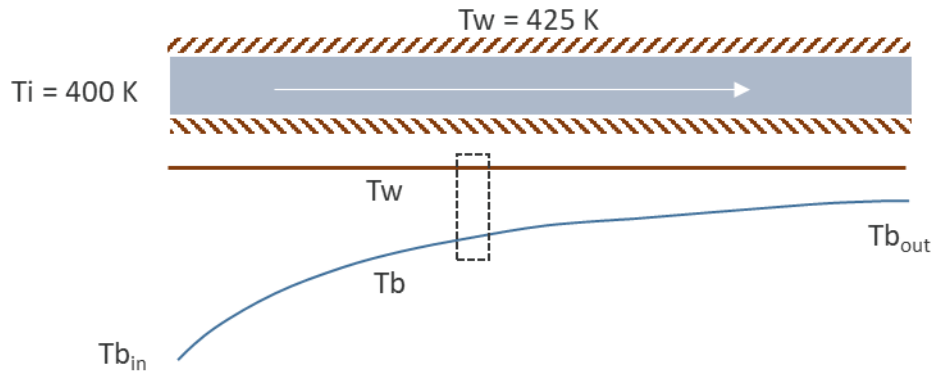


*Figure 2: Thermal boundary conditions and bulk flow temperature variation.*

## 2.1. Geometry Setup and Meshing

The helical pin fin geometry is shown in Figure 3 and a computer aided design (CAD) rendering is shown in Figure 4. Design parameters are discussed in detail in Section 3.2.

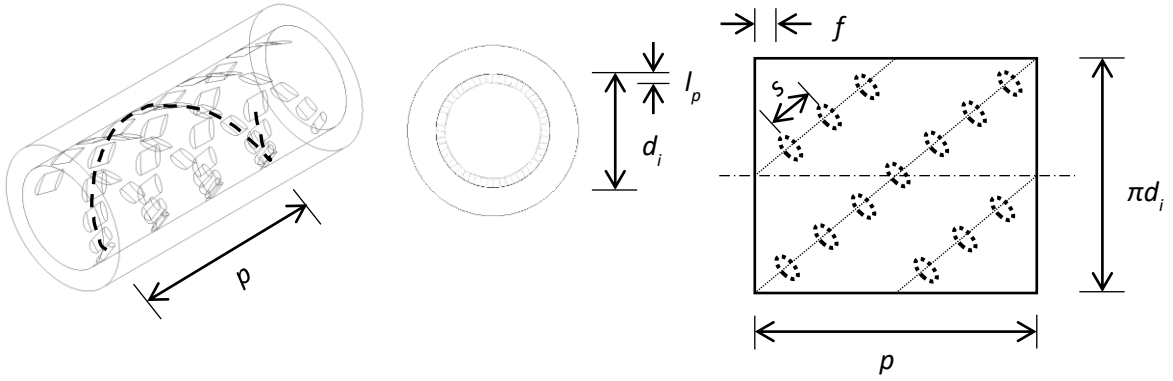


*Figure 3: Drawing schematics of helical pin fin designs.*

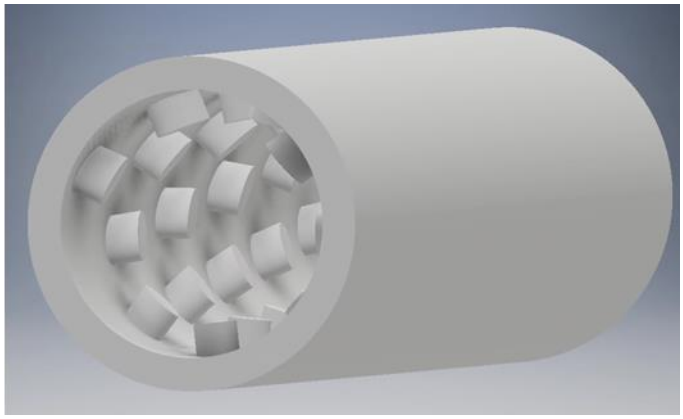

*Figure 4: CAD rendering of helical pin fin tube design.*

Images of the fluid domain mesh are displayed in Figure 5. The domain was meshed with tetrahedrons using a patch conforming algorithm. On the top row (a-b), images are shown of the cylindrical surface with detail around the cooling pin. The nominal element size was 0.2 mm. Fifteen inflation layers with a growth rate of 1.2 were applied at the outer tube wall and the pin fins. The first layer thickness was $5.8 \times 10^{-4}$ mm. The inflation layers are visible in the second row of images (c-d), where the tube inlet is displayed. In the bottom row (e-f), a section view of the mesh is shown with a detail view around a pin feature. In the refined regions, the nominal element size is 0.06 mm. Grid independence was verified by conducting a simulation with a baseline pin design. The baseline mesh had $1.71 \times 10^{7}$ cells. The cell count was increased by 20% by adjusting the nominal cell size and remeshing. The change in $Nu$ predicted was less than 1%.

## 2.2. Simulation Benchmark Studies

Several benchmark simulations were performed prior to modeling the helical pin fin geometry. Smooth tube simulations were evaluated to explore effects of unheated starting length, and turbulence model. Inline pin fins were studied to identify entrance length trends. The effect of tube length on area-averaged Nusselt number was determined including the length of pin-finned tube required to achieve a fully-developed flow. A study with inline pin fins found that the wall-averaged Nu varied by less than 4% for tube lengths greater than 12.7 mm. Results for $Nu$ vs. $L$ are plotted in Figure 6. Simulations were run with this tube length so that each trial simulation could be obtained in a timely manner. It was noted earlier that the SST k-$\omega$ model was utilized for turbulence closure. Results relevant to this decision are provided in Table 2. Here, the SST k-$\omega$ model was demonstrated to have better agreement with Petukhov's correlation for a smooth tube than the realizable k-$\epsilon$ model.

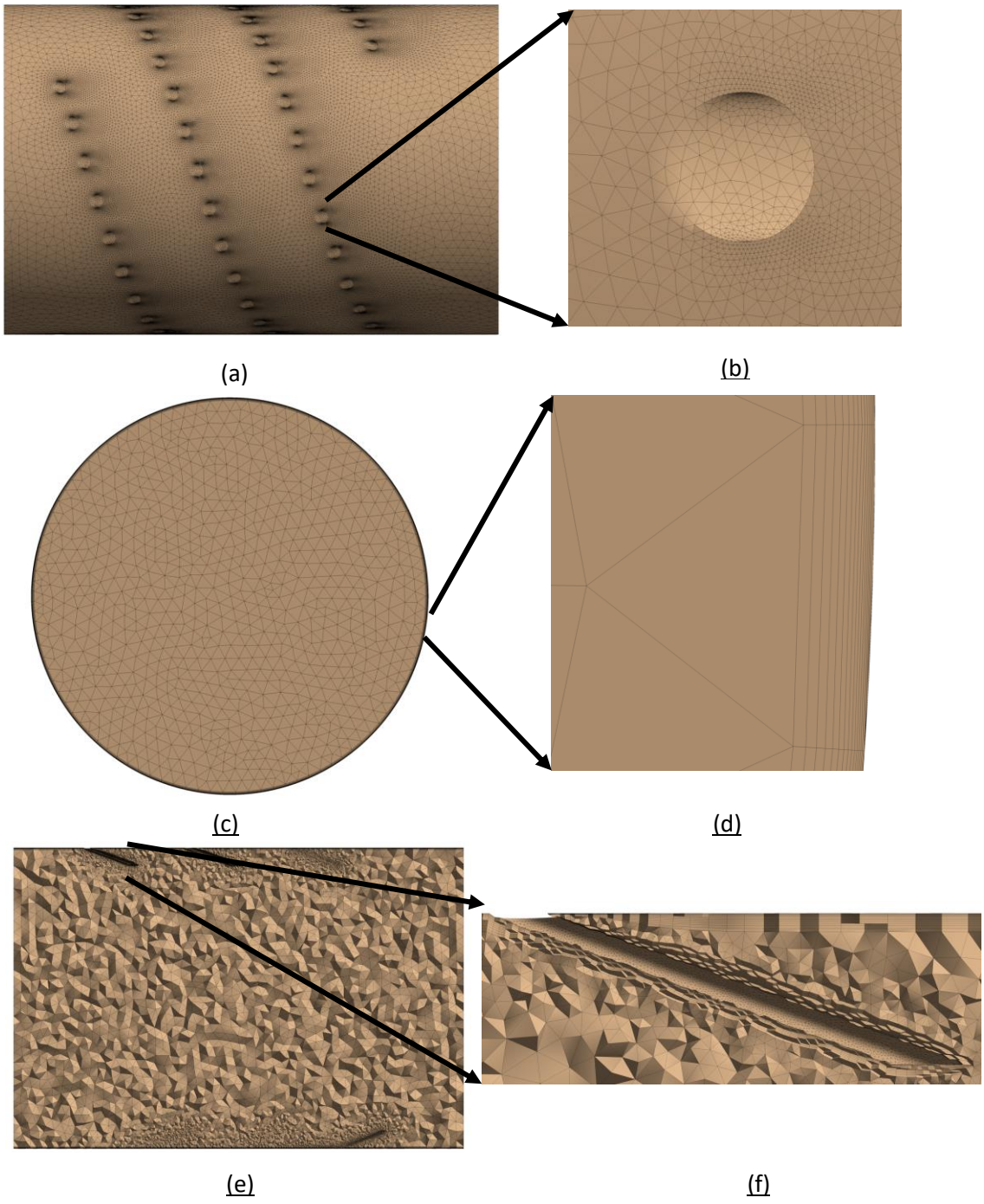


Figure 5: Images of the simulation mesh are displayed. Top row (a-b), images are shown of the cylindrical surface with detail around the cooling pin. Second row (c-d), images are shown of the tube inlet and wall boundary refinement. Bottom row (e-f), a section view of the mesh with complete elements is shown with a detail view around a pin feature

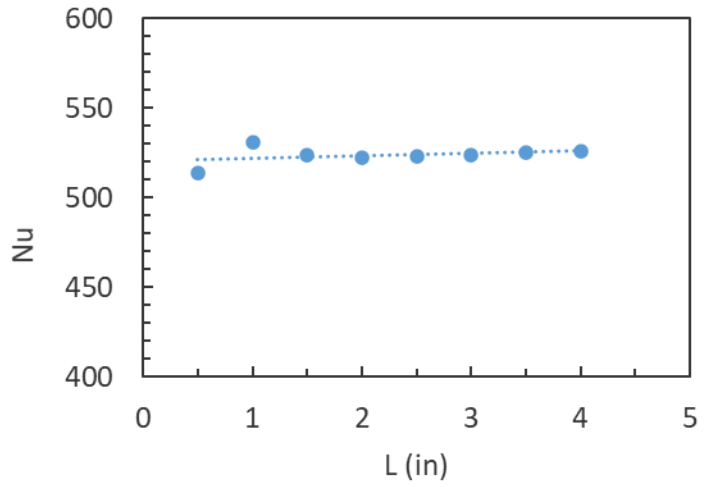


*Figure 6*: $Nu$ as a function of $L$ for tubes with inline pin fins. Dashed line represents linear fit to data points.

*Table 2: Effect of turbulence model on area averaged Nu.*

| | |
|---|---|
| Nu: Petukhov's correlation | 148 |
| Nu: Rkε model | −6% |
| Nu: SST-kω model | −3% |

## 2.3. Data Reduction

The Nusselt number and the friction factor were calculated from the simulation results.

The wall heat flux was expressed as a classical log-mean temperature rate law, which is applicable for the uniform wall temperature case. The calculations were performed over the simulation volume containing the final complete helical pass.

$$Q" = h\,\Delta T_{lm} \tag{3}$$

$$\Delta T_{lm} = \frac{\left(T_w - T_{b,i}\right) - \left(T_w - T_{b,o}\right)}{ln\left(\frac{\left(T_w - T_{b,i}\right)}{T_w - T_{b,o}}\right)} \tag{4}$$

$$h = Q"/\Delta T_{lm} \tag{5}$$

$$Nu = hd/k \tag{6}$$

The flow friction factor was calculated from the simulation results using the Darcy-Weisbach equation.

$$\Delta P = f\, l \frac{\rho u^2}{2D} \tag{7}$$

## 2.4. Optimization-Inspired Design Search

### 2.4.1. Method

The Direct Optimization package in ANSYS Workbench was utilized in conjunction with ANSYS Fluent. The geometry was defined parametrically in a CAD file and linked to the CFD and optimization software. The optimization approach was selected to be Adaptive Single Optimization (ASO). ASO consists of the following components: an Optimal Space-Filling (OSF) design of experiments (DOE) [21], a Kriging response surface, and the Mixed-Integer Sequential Quadratic Programming (MISQP) optimization algorithm with domain reduction to locate the global optima. At each optimization step, the algorithm retained 75% of the domain for the subsequent iteration.

Prior to selecting ASO, various optimization schemes were evaluated including a multi-objective genetic algorithm and single and multi-parameter methods. A single objective optimization was pursued, requiring the definition of an appropriate thermal performance parameter. Due to complexities associated with reproducing identical conditions in the experiments to those simulated in the CFD, experimental results are compared to the scaled CFD dataset in a multi-objective manner.

### 2.4.2. Objective Function

Four thermal performance factors, $TPF$, were evaluated as objective functions. These criteria are displayed in Figure 7. The first, $TPF$, is the classical thermal performance factor which for $TPF > 1$, indicated an increase in heat transfer at constant pumping power and constant heat transfer area. $TPF_2$ is the classical thermal performance factor weighted by the pin fin volume. To allow simulations with different tube lengths, $TPF_4$ was introduced, in which the pin fin volume was divided by the tube length. $TPF_3$ is different than $TPF_4$ in that the thermal performance factor is normalized by the total tube volume. $TPF_3$ would be valuable to a design engineer when optimizing the entire heat exchanger. $TPF_4$ was selected as the objective function for the present optimization. The selected thermal performance factor strongly affects the optimum parameters found by the algorithm. Ultimately, based on the experimental results, the $V/V_0$ parameter (introduced in Section 3.3) is preferred over $TPF_2$, $TPF_3$, or $TPF_4$ since these parameters introduce dimensionality into the objective function and are not derived from a physics-based model. Future optimization efforts will utilize the $V/V_0$ parameter.

When exploring the various objective functions, it was identified that the selection of an objective function is governed by the design goals. The standard thermal performance factor, $TPF$, is the most widely used factor and indicates a performance improvement when the change in area is minimal. $TPF > 1$ indicates that an enhanced heat exchanger with equal pumping power and heat transfer area would have an increased heat rate. It is important to note that any performance factor, including the $TPF$, is at best a screening parameter. A design with a TPF < 1 could be useful to the designer provided that $Nu/Nu_0$ is greater than 1 and the rise in $f/f_0$ is not excessively large. Frequently, heat exchanger designers accept a $f/f_0$ penalty simply to achieve a $Nu/Nu_0$ gain in the same sized heat exchanger. A future technoeconomic analysis could determine if this approach is cost-effective. Such a study would include the contributions of $Nu/Nu_0$, $f/f_0$, surface area, and fin efficiency.

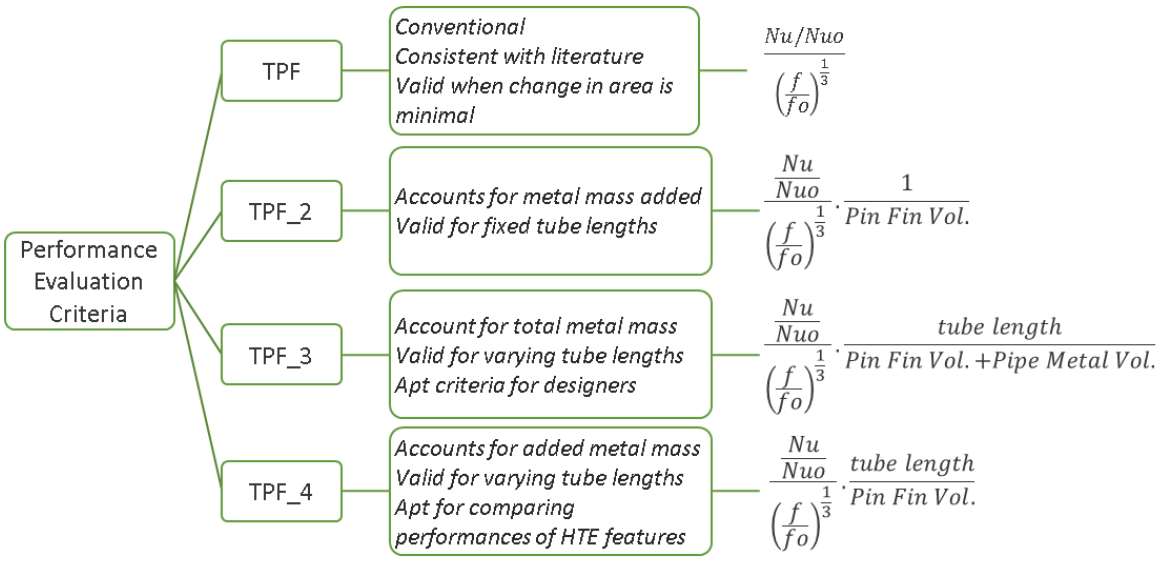


*Figure 7: Thermal performance criteria considered for the optimization component of this study.*

# 3. Experimental Approach

## 3.1. Test Facility/Method

The heat exchanger tube designs were tested in the Heat Exchange and Experimental Testing (HEET) Facility at NETL. The test facility and experimental approach have been introduced previously [3, 22]. A flow schematic of the test facility is shown in Figure 8 panel (a) and a picture in panel (b).

The experiments were conducted using the Wilson plot approach, where the measured heat exchanger overall thermal resistance is plotted as a function of the calculated internal convective resistance.

The experimental technique has been previously reported for use in the HEET rig [3] and the approach is summarized here.

Under conditions of small property variations, negligible conjugate conduction, and small heat transfer to the environment, the total resistance ($R_{ov}$) from the hot fluid to a cold fluid in a heat exchanger is:

$$R_{ov} = \frac{LMTD}{Q} \tag{8}$$

Where $LMTD$ is the log mean temperature difference and $Q$ is the heat rate. The overall resistance between the hot stream and the cold stream may also be written as the sum of the convection resistance at the cold side wall ($R_c$), the conduction resistance in the tube wall ($R_w$), and the convection resistance at hot side wall ($R_h$).

$$R_{ov} = R_c + R_w + R_h \tag{9}$$

The convection resistances are expressed as $R_c = 1/\eta h_c A_c$ and $R_h = 1/h_h A_h$ where $h_c$ is the heat transfer coefficient at the cold side, $A_c$ is the cold side area, $h_h$ is the heat transfer coefficient at the hot side, and $A_h$ is the hot side area. $R_c$, $R_w$, and $R_h$ are each unknown. However, $R_{ov}$ can be calculated from experimental temperature measurements utilizing Equation (8). The experiments are performed so that $R_c$ varies while $R_w$ and $R_h$ remain constant.

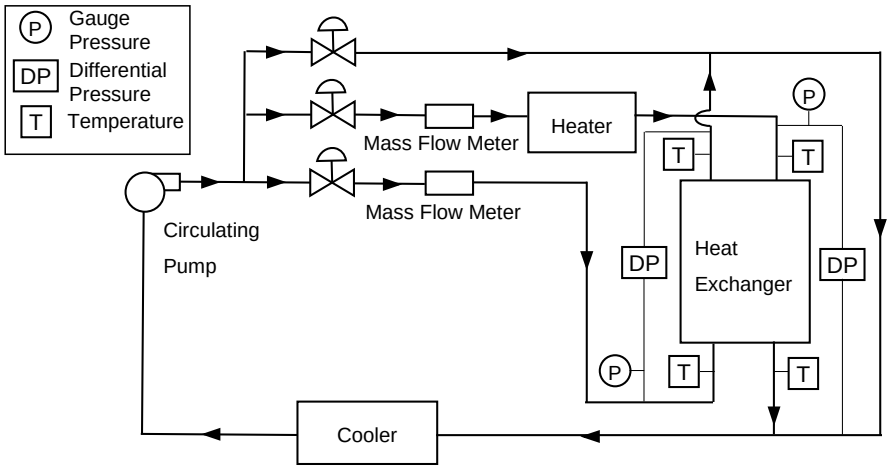


(a)

(b)

*Figure 8:* HEET rig flow schematic (panel (a)) and photograph (panel (b)).

The slope of this line, $R_c/R_{c0}$ is given in Equation (10) from which the Nusselt number may be calculated as shown in Equation (11).

The Wilson plot is now formed by plotting $R_{ov}$ as a function of $R_{c0}$. A typical plot is shown schematically in Figure 9. It must be emphasized that $(R_c/R_{c0})$ is the slope of the line and the y-intercept is $R_w + R_h$. If the calculated values, $R_{c0}$, equal the unknown experimental value, $R_c$, then $R_c/R_{c0}$ = 1 and the $R_{ov}$ vs. $R_{c0}$ line has a slope of 1. Otherwise, the $R_c/R_{c0}$ value can be used to calculate $Nu/Nu_0$.

$$\frac{R_c}{R_{c0}} = \frac{\left(\frac{1}{\bar{\mathrm{h}}\mathrm{A}}\right)}{\frac{1}{(\mathrm{hA})_0}} = \frac{D}{\eta A k_f \overline{Nu}} \frac{A_0 k_f Nu_0}{D} = \frac{A_0 Nu_0}{\eta A \overline{Nu}} \tag{10}$$

$$\frac{\overline{Nu}}{Nu_0} = \frac{\mathrm{R_{c0}}}{R_c} \frac{A_0}{\eta A} \tag{11}$$

It is important to note that the average Nusselt number $\overline{Nu}$ measured by the experiments is equal to the Nusselt number, $Nu$, predicted by the simulations. $Nu$ is the circumferential and pitch-averaged Nusselt number. Thus, $\overline{Nu}$ is a discrete average of $Nu$ over the number of helix rotations required to span the length of the tube. Since the flow is fully-developed, the axial property variation is small. Further, the features are uniformly distributed. Consequently $\overline{Nu} = Nu$. From this point forward, all results will be referenced by $Nu$ due to this equality.

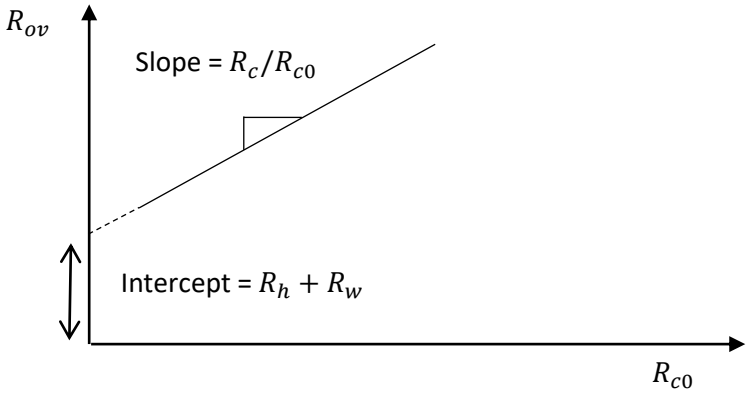


Figure 9: Schematic illustration of Wilson plot.

Hydrodynamic results, including the friction factor, are calculated by measuring the pressure drop across the tube with a differential pressure transducer.

Uncertainty in the friction factor, Nusselt number, and thermal performance factor were determined using the Kline and McClintock approach [23]. Details on transmitter uncertainties are available in a prior work [3]. To report uncertainties at a 95% confidence interval, it is assumed that all manufacturer uncertainties are reported at one standard deviation. These measurement uncertainties are doubled before entry into the propagation of error analysis. This yields a 95% confidence interval in the reported uncertainties.

Test conditions for the present study are shown in Table 3. Test condition 1 was typical of the temperature and pressure encountered at the low-pressure outlet of a $sCO_2$ cycle low temperature recuperator and were previously considered in the experimental rig [3]. Test condition 4 approached the conditions of the high-pressure line in the low temperature recuperator [14, 24, 25], but the rig design pressure limit prevented operation at the higher pressures.

*Table 3: Test conditions for present study.*

| | Test Condition 1 | Test Condition 4 |
|---|---|---|
| **Tube** | | |
| Inlet Pressure [MPa] | 8.69 | 15.5 |
| Mass Flow Rate Range [kg/hr] | 32.0 – 103.1 | 48.2 – 89.5 |
| Inlet Temperature [K] | 360.9 | 397.6 |
| Reynolds Number Range [-] | $7.73 \times 10^4 – 2.49 \times 10^5$ | $9.14 \times 10^4 – 1.70 \times 10^5$ |
| **Shell** | | |
| Mass Flow Rate Range [kg/hr] | 226.8 | 226.8 |
| Inlet Temperature* [K] | 422 | 463.7 |
| Reynolds Number [-] | $1.5 \times 10^5$ | $1.27 \times 10^5$ |
| *Approximate, average shell temperature held constant across tests. | | |

## 3.2. Test Articles

*Test article parameters, including design and "as-printed" values are reported in Table 4. In this table, dimensions from the CAD geometry are presented in the "Design" columns and measurements from the CT scan are displayed in the "as-printed" columns.*

*CAD geometry and CT scan profiles of the test articles are displayed in*

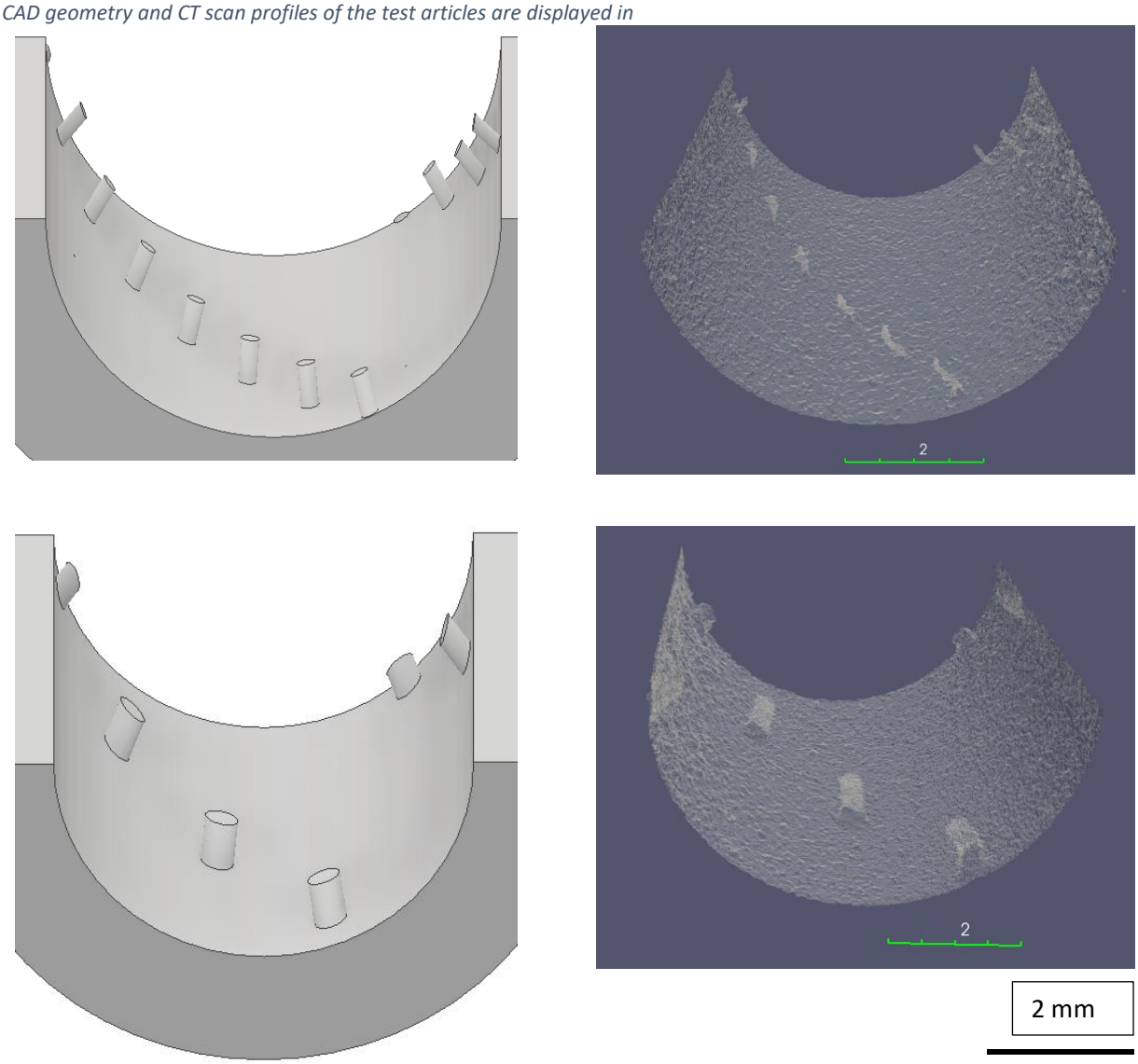


Figure 10.

*Several observations are important to note concerning the reported parameters. First, the printed pin diameters are smaller than the design parameters. This is attributed to poor powder fusion for the small feature sizes. For test article 1, the fin length is also shorter. Agreement for the wall angle is somewhat better but some uncertainty arises due to curvature in the fins. Features exhibiting curvature are shown*

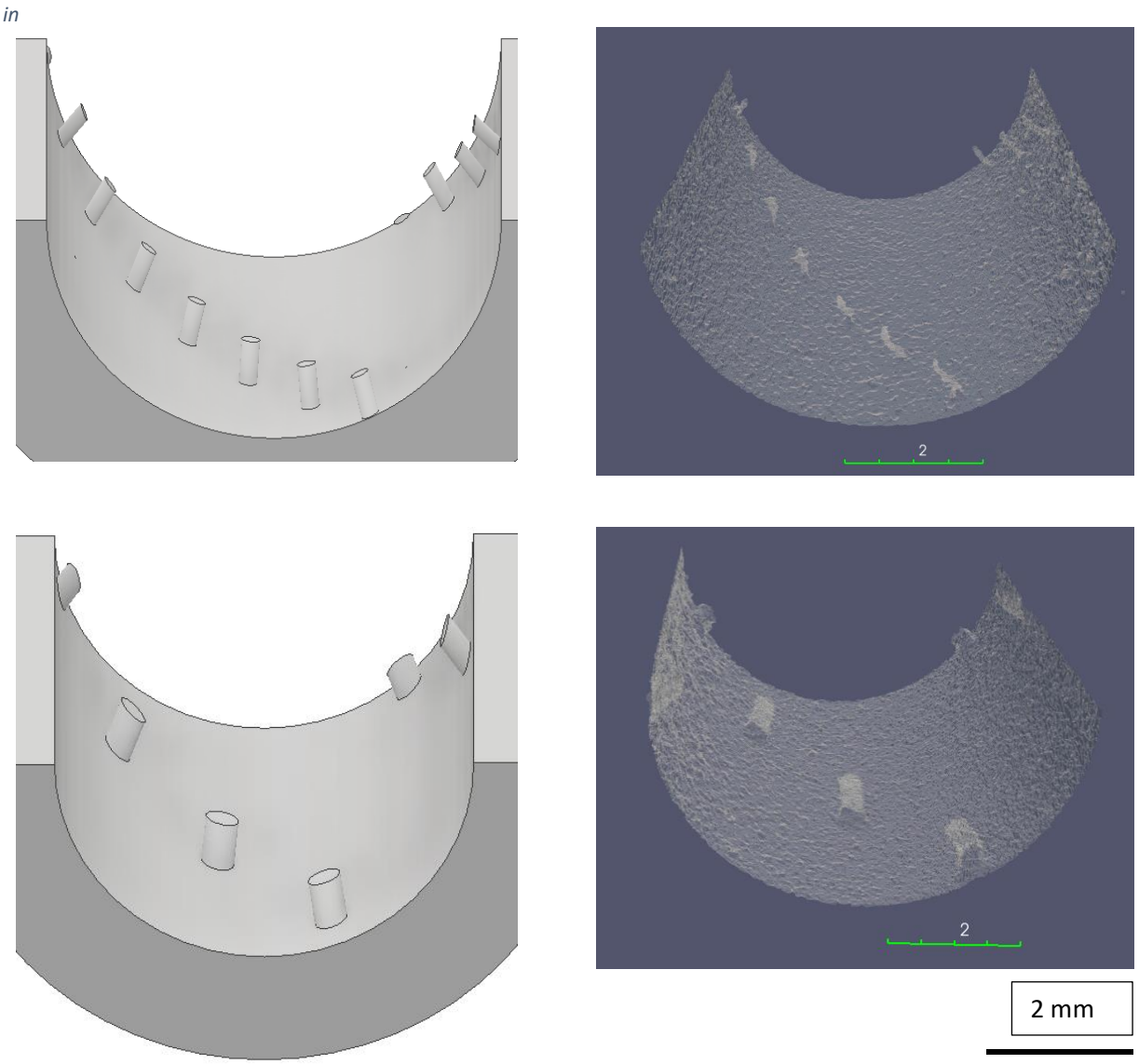


Figure 10 panel (a). While the dimensional spacing between the fins equaled the design value, the non-dimensional spacing (relative to fin diameter) increased due to the decrease in pin size.

$A/A_0$ is within 3% percent for Tube 1 and within 0.1% for Tube 2 due to the large ratio of un-finned area (primary heat transfer area) to total surface area. For both tubes, $M/M_0$, increases 4% for Tube 1 and 8% for Tube 2 due to the tube printing process tolerances and additional volume filled by sintered non-fused particles.

In summary, the printed test articles showed deviations from the design CAD geometries. All results in this analysis conducted from this point will use the “as-printed” parameters.

*Table 4: Test article parameters. CFD optimum test article parameters shown for comparison.*

| | TPF 4 | Tube 1 | | Tube 2 | |
|---|---|---|---|---|---|
| Exp/CFD | CFD | Exp | | Exp | |
| | | Design | As-Printed | Design | As-Printed |
| Major Diameter [mm] | 0.25 | 0.25 | 0.11 | 0.5 | 0.33 |
| Minor Diameter [mm] | 0.25 | 0.25 | 0.11 | 0.5 | 0.33 |
| Fin Length [mm] | 1 | 1 | 0.68 | 1 | 1.02 |
| Wall Angle [°] | 20 | 20 | 24.8 | 20 | 17.6 |
| No. Helix Paths | 3 | 3 | 3 | 3 | 3 |
| Helix Pitch [-] | 4.5 | 4.5 | + | 4.5 | + |
| Helix Spacing [-] | 6 | 6 | 13.5 | 6 | 9.1 |
| ID [mm] | 6 | 6.22 | 6.22 | 6.22 | 6.22 |
| Tube Length [mm] | 12 | 142 | 142 | 142 | 142 |
| OD [mm] | 8 | 9.53 | 9.53 | 9.53 | 9.53 |
| $A/A_0$ | 1.070 | 1.068 | 1.037 | 1.068 | 1.067 |
| $M/M_0$ | 1.002 | 1.001 | 1.042 | 1.002 | 1.078 |

[+] Not measured

### 3.3. Fin Efficiency and Thermal Performance Factor

The overall fin array efficiency was calculated using standard equations for uniform cross-section extended surfaces [20].

The individual fin efficiency, $\eta_f$, for a pin fin with a convective tip is

$$\eta_f = \frac{\sqrt{(hPk_m A_{xs})}}{hA_{fin}}((\sinh nL + \left(\frac{h}{nk_m}\right)\cosh mL)/(\cosh nL + \left(\frac{h}{nk_m}\right)\sinh(nL)) \quad (12)$$

where $n^2 = hP/k_m A_{xs}$, $P$ is the perimeter, $A_{xs}$ is the cross-sectional area, $A_{fin}$ is the fin surface area, $L$ is the fin length, and $k_m$ is the metal thermal conductivity.

The overall efficiency, $\eta$, is calculated

$$\eta = (A_s \eta_f + A_p)/(A_s + A_p) \tag{13}$$

where $A_p$ is the primary surface area (the tube area not covered by pins) and $A_s$ is the secondary or fin area.

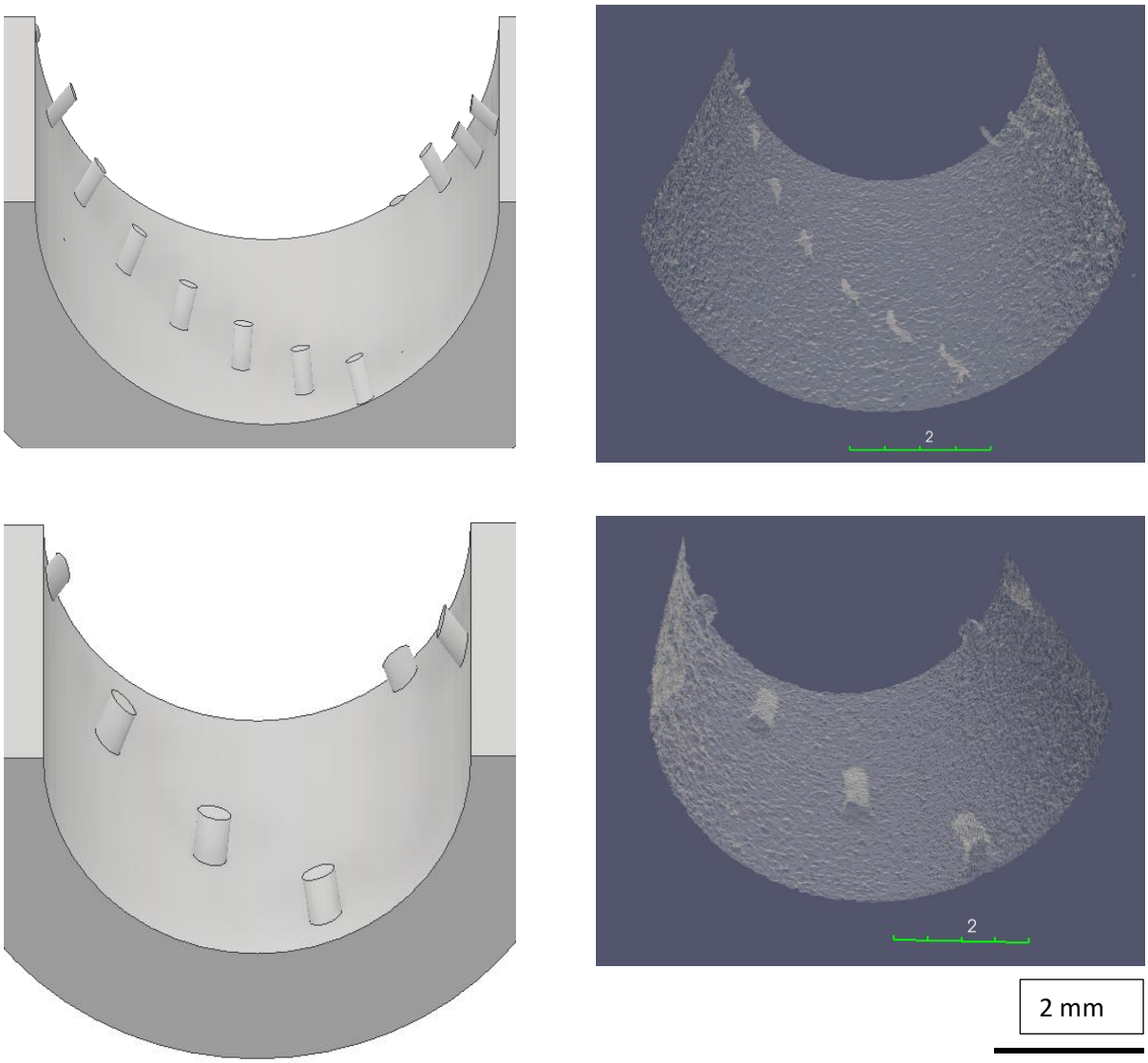


*Figure 10: Tube 1 CAD geometry (panel (a)) and CT scan (panel (b)). Tube 2 CAD geometry (panel (a)) and CT scan (panel (b)).*

An important consideration in the present study is the thermal performance factor. Three performance factors were considered for the experimental effort: classical thermal performance factor, $TPF$; heat

exchanger volume reduction factor, $V/V_0$; and $TPF$, scaled by fin volume. Derivations of the first two performance parameters are available in prior work [3, 26].

As defined earlier, the classical thermal performance factor $TPF$ is defined:

$$TPF = (Nu/Nu_0)/(f/f_0)^{1/3} \tag{14}$$

$TPF > 1$ indicates that an enhanced heat exchanger would have a higher heat duty at fixed pumping power and fixed internal heat transfer area than a smooth tube heat exchanger. We note that the classical thermal performance factor assumes an overall fin efficiency of $\eta = 1$.

Heat exchanger volume reduction factor, $V/V_0$ is defined:

$$\frac{\mathrm{V}}{\mathrm{V}_0} = \frac{(f/f_0)^{1/2}}{(\eta\, Nu/Nu_0)^{3/2}} \frac{A_n}{A_a} \frac{M}{M_0} \tag{15}$$

Where $A_n$ is the internal surface area of a single smooth tube (assuming the heat exchanger can have multiple parallel tubes), $A_a$ is the internal surface area of a single rough tube, $M$ is the total material volume, and $M_0$ is the total material volume for a smooth tube.

$V/V_0 < 1$ indicates that the enhanced heat exchanger would require less volume at fixed pumping power and fixed heat duty than a smooth tube heat exchanger.

The final performance factor, $TPF^* = TPF/(Fin\ Volume/Length)$, scales $TPF$ by the fin volume and length, giving designs with smaller pins a higher value. It is noted that $TPF^*$= $TPF_4$ from the optimization study.

# 4. Results and Discussion

## 4.1. Optimization-Guided Design Exploration

It is important to understand that the final design (parameters reported in the $TPF_4$ column of Table 4) was inspired by multiple direct single objective optimization campaigns. This section outlines the results from two optimization runs that helped to define the final design.

*In*

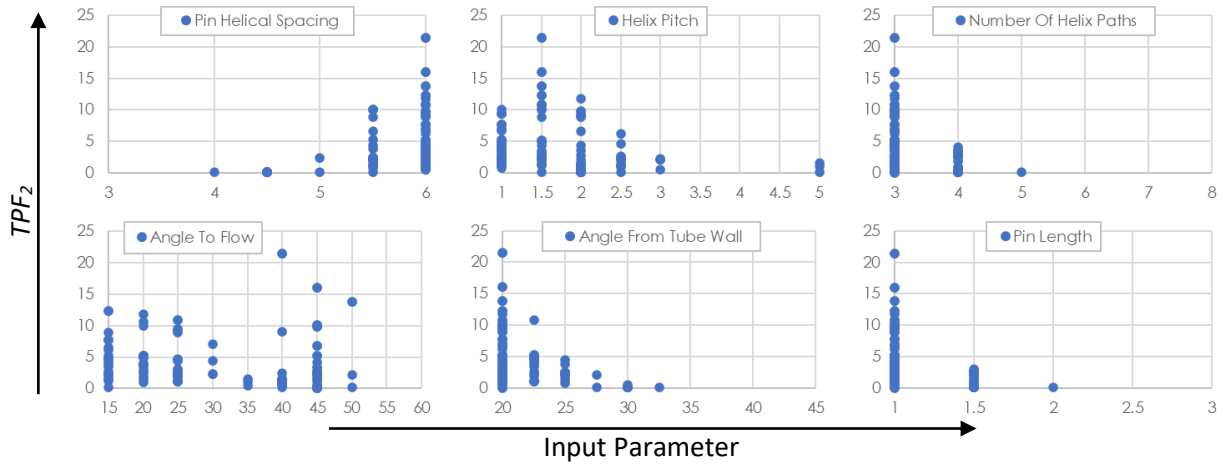


Figure 11, $TPF_2$ is plotted versus input parameter for six parameters of interest: pin helical spacing, helix pitch, number of helix paths, angle to the flow, angle from the tube wall, and pin length.

As displayed in the figure, $TPF_2$ reached an optimum for pin helix spacing at the upper parameter bound, 6. $TPF_2$ reached an optimum when the number of helix paths, angle from the tube wall, and pin fin length reached their lower bounds of 3, 20°, and 1 mm, respectively.

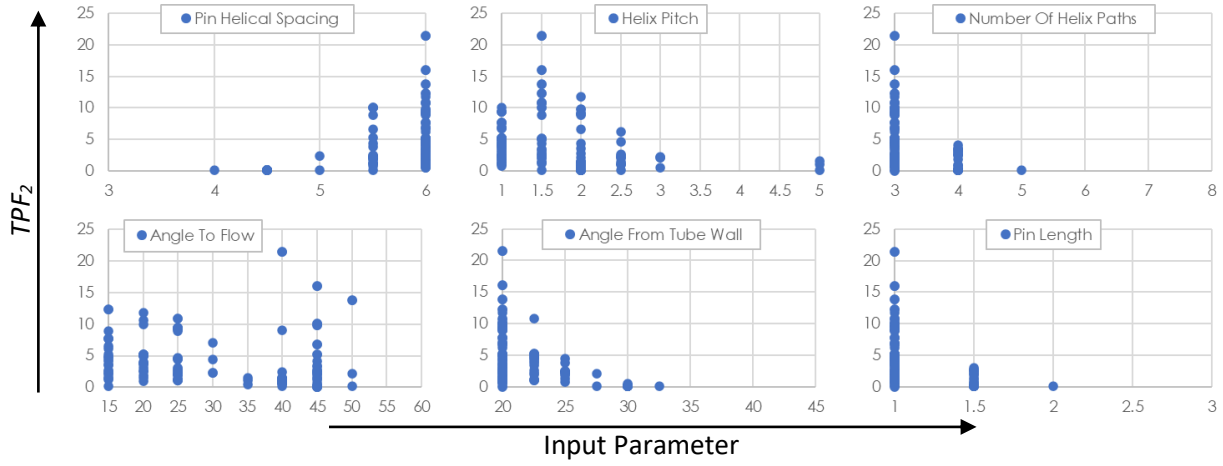


*Figure 11: $TPF_2$ versus input parameter for pin helical spacing, helix pitch, number of helix paths, angle to flow, angle from tube wall, and pin length.*

A peak in $TPF_2$ indicates an optimal helix pitch of 1.5. The distribution in $TPF_2$ versus the angle to the flow results appeared bimodal with high performance at angles of 15° and 40°. For pins with circular cross-sections the angle to the flow is irrelevant. Also, as determined in this campaign, but not shown here is the result that the minimum fin diameter optimizes the design.

While optimizing the design for $TPF_2$, it was identified that the thermal performance factor needed to be normalized by the tube length. Furthermore, only the helix pitch and the angle to the flow needed to

vary in the optimization since the other parameters could be fixed at their respective lower or upper bounds.

The scaling by tube length was performed and $TPF_3$ and $TPF_4$ were introduced. The objective function was set to be $TPF_4$, where the traditional $TPF$ is normalized by the fin volume. The effect of the normalization was that the optimal result was obtained at higher non-dimensional helix pitches (4.5). This result is visible as shown in Figure 12. The change in the optimum parameter resulted from the higher relative weighting of the small fin volume on $TPF_4$ rather than the total volume.

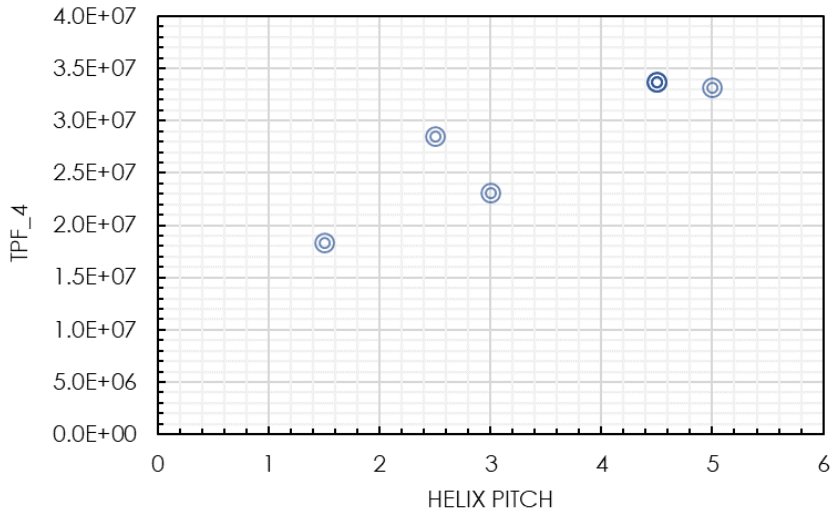


*Figure 12: Thermal performance factor #4 versus helix pitch.* Optimal point bolded.

At this point, the design exploration was concluded, and the best-performing design was selected as reported in Table 4.

## 4.2. Experimental Results

The experimental results are now presented and compared to the numerical results. First, Wilson plot and pressure drop data for each tube and test condition are reported. Then, the thermal performance of the optimized design is reported by considering trends in Nusselt number, friction factor, overall fin efficiency, and thermal performance factors. Finally, the test heat exchanger is compared to other heat exchanger technologies on a specific mass basis.

In Figure 13, $R_{ov}$ is plotted as a function of $R_{c0}$ generating a Wilson plot for each test article and test condition. Each plot consists of five points. It is recalled that the slope is equal to $R_c/R_{c0}$. From Equation (11), it is apparent that $Nu/Nu_0$ is proportional to the inverse of the slope. Thus, a decrease in slope indicates an increase in $Nu$. As shown in Figure 13, the slope (nominally 0.5) is largely insensitive to changes between the test condition or the tube.

In Figure 14, results for $\Delta P$ versus $Re$ are shown for each tube and test condition combination. The uncertainty in $\Delta P$ is 0.2%, thus the error is less than the size of the markers and is not indicated with

error bars. For clarity, quadratic curve fits are shown to interpolate results between the data points. This functional trend is expected since the pressure drop depends on the tube velocity to the second power.

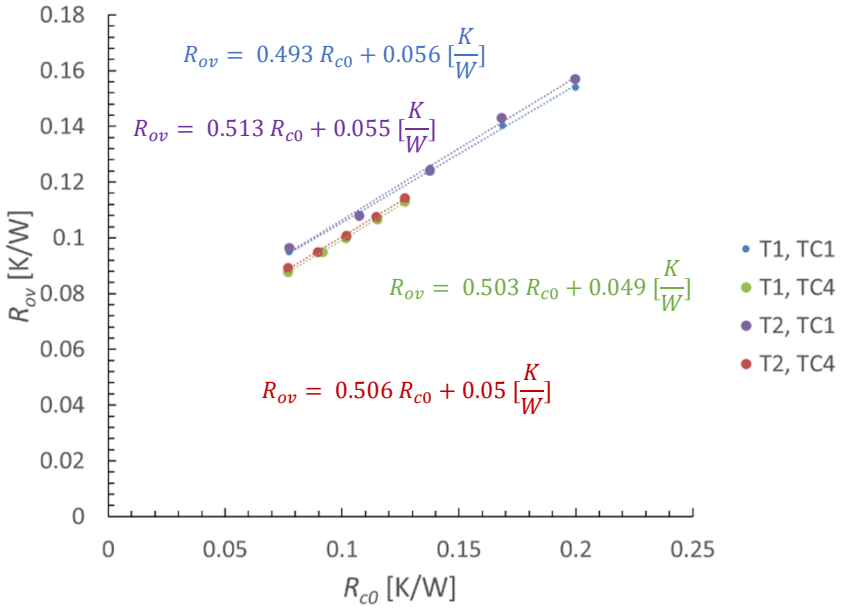


*Figure 13: Plots of $R_{ov}$ versus $R_{c0}$ (Wilson plots) for each test condition and tube design considered.*

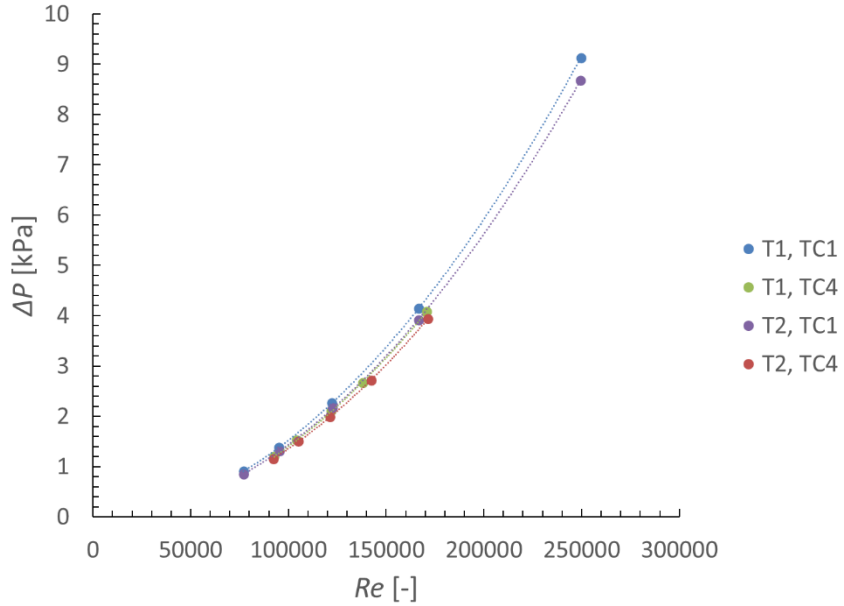


*Figure 14: ΔP versus Re for each test condition and tube design considered. Quadratic curve fits shown for clarity.*

In Figure 15, $Nu$ is plotted as a function of $f$. Experimental points for Tube 1 and Tube 2 at conditions 1 and 4 are shown. For comparison, top performing designs, A and B, from ATE2020 [3] are shown at test condition 1. CFD trial points are displayed as well. The condition that optimized $TPF_4$ is indicated by a separate marker. Curves indicate the locus of $Nu$ and $f$ values that yield $TPF = 0.9$, 1, and 1.1. The experimental dataset for all points, except the CFD trial points, is shown in Table 5.

The following observations are important to make concerning the results in this figure. First, Tube 1 and Tube 2 have equal performance, within a 95% confidence interval.

The optimization-inspired helical pin tube has a friction factor which was at least four times smaller than the prior baseline designs, with the Nusselt number nominally equal. The experimental, optimization-inspired test articles had a 14% higher Nusselt number than the CFD trial points at equal friction factor. Furthermore, Tube 1 (equal parameters to the optimal CFD design) had $Nu$ = 511, $f$ = 0.129, both larger than the CFD prediction, $Nu$ = 311 and $f$ = 0.052.

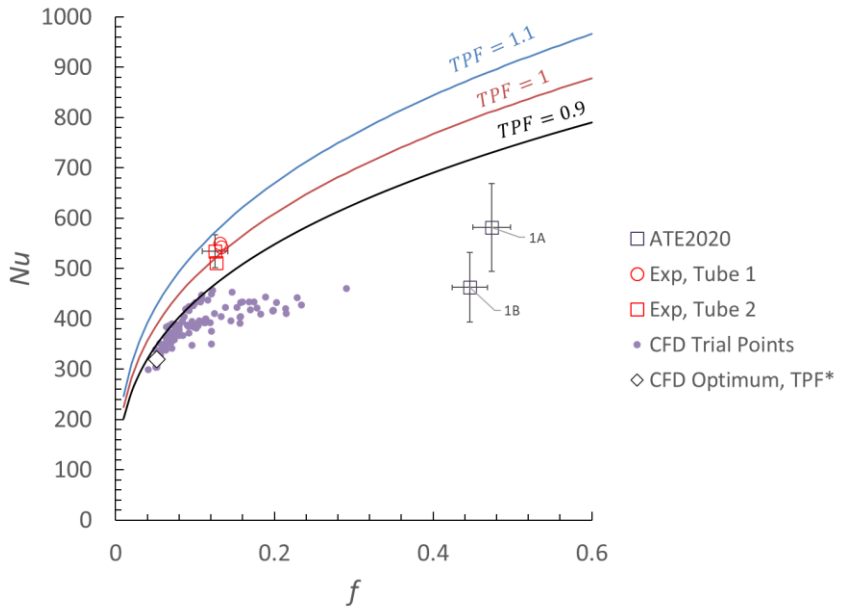


*Figure 15: Nu as a function of f for each test condition considered. Present experimental results at each test condition and for Tube 1 and Tube 2 are presented. CFD results across a range of parameters are shown as purple points and represent a Pareto front. The CFD point which optimizes thermal performance factor four is indicated by an open diamond. Prior experimental results* [3] *are displayed as well.*

Deviation from the design intent and surface roughness due to additive manufacturing yielded test articles with higher performance than the CFD design. The CT scan imaging indicated that the morphology of the pin fin features was altered in the additive manufacturing process and surface roughness was introduced. It is important to recall that the CFD simulation did not account for either effect. For Tube 1, the fin diameter decreased by 50% and the length decreased by 32%. For Tube 2, the fin length equaled the design length but the fin diameter decreased by 34%. In this scenario, the deviations from design intent and surface roughness increased the thermal performance relative to the smooth, non-deformed design.

An important discussion point, as introduced in Section 2, is how to interpret the computational results when $TPF < 1$. Here, $TPF$ is less than 1 when the optimized CFD results are scaled to experimental conditions. However, this does not negate the value of the present results. The results indicate that the helical pin architecture must suffer a pumping power penalty at the expense of its Nusselt number augmentation. Furthermore, the experimental results demonstrate a $TPF$ marginally greater than 1 indicating that deviation from design intent and surface roughness can further improve the present design.

Shown in Figure 16 is the overall fin efficiency for the present test articles (Tube 1 and Tube 2), the prior study (ATE A-C), and the CFD result optimizing $TPF^*$. The process conditions for Tube 1, Tube 2, and the CFD are at test condition 4, while process conditions for ATE2020 are at test condition 1. As shown in Figure 15, $Nu$ and $f$ at test condition 1 and test condition 4 are each equal within a 95% confidence interval. Thus, a direct comparison between results at test conditions 1 and 4 is permissible both for the overall fin array efficiencies and the thermal performance results in Figure 17. Regardless, Tube 1 and Tube 2 show a marked improvement in fin efficiency over ATE2020 A-C. Relative to the CFD results, Tube 1 has a fin array efficiency equal within 0.1% while Tube 2 has a 1% smaller overall fin efficiency.

Several observations are important to make concerning these results. First, the overall fin efficiency is dominated by the prime surface heat transfer area (tube surface) and not the added fin area. This is expected due to the small pin size and the sparse distribution. Second, the close agreement indicates that a change in pin volume and surface area due to the additive manufacturing process has only a small impact on the overall fin efficiency. Finally, fin efficiency has a small impact (2 to 4%) on the resulting Nusselt number and the thermal performance factor.

In Figure 17, three performance factors (introduced in Section 3.3) are plotted for Tubes 1 and 2, and the ATE2020 tubes A, B, and C. It is noted that ATE Tube C has $f$ = 1.06 and is not displayed in Figure 15. Including this point would have skewed the chart away from the other data. Error bars show the 95% confidence interval. The error bars shown for Tube 1 are typical of the points for Tube 2 with the other error bars omitted for clarity.

It is recalled that an increase in $TPF$ indicates an increase in heat transfer for the enhanced design at fixed area and pumping power, an increase in $V_0/V$ represents a decrease in heat exchanger volume at fixed heat rate and pumping power, and an increase in $TPF*$ indicates an increase in $TPF$ or a decrease in pin fin volume.

The following findings are important to make concerning these results. Tube 1 (optimization-inspired design) yields an improvement over the CFD of 27% for $TPF$ and $TPF*$ and 40% for $V0/V$. Tube 2 yields a similar improvement over the CFD for each performance factor except $TPF*$, where a decrease of 38% is observed.

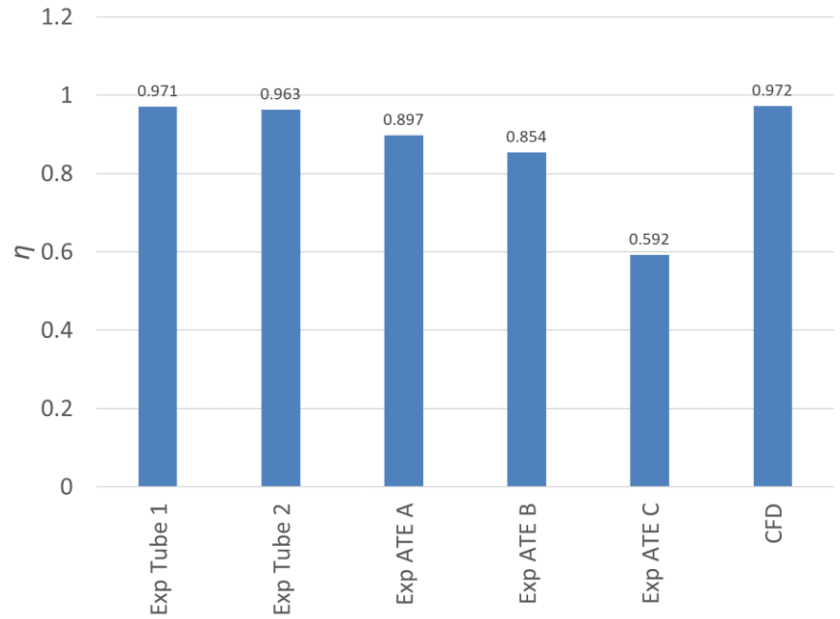


*Figure 16: Overall fin array efficiency for present test articles (Exp Tube 1 and Exp Tube 2), prior study (ATE A-C), and CFD result optimizing TPF*. Process conditions for Exp Tube 1, Exp Tube 2, and CFD are at test condition 4.*

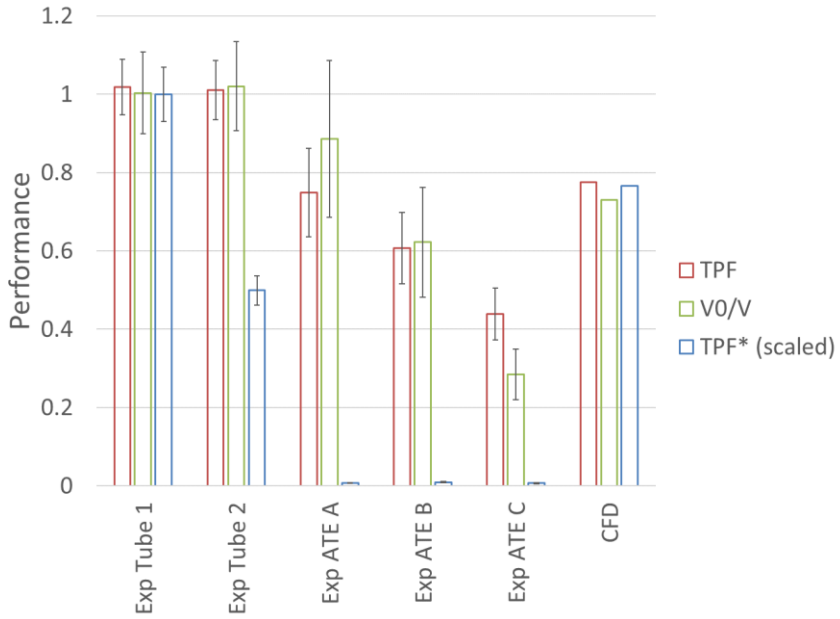


*Figure 17: Thermal performance factor, $TPF = (Nu/Nu_0)/(f/f_0)^{1/3}$, reciprocal of volume reduction factor, $V0/V$, and thermal performance factor divided by fin volume, $TPF^* = TPF/(Fin\ Volume/Length)$ scaled by value for test article and test condition 11.*

For $TPF$, the CFD optimal design and experiment designs 1 and 2 showed improvement relative to previous experimental results for baseline tubes A, B, and C [3]. Uncertainty in baseline tube A for $V_0/V$ is relatively large. Thus, it is not clear if Tube 1 and Tube 2 have higher $V_0/V$ relative to ATE tube A. $TPF^*$ is dominated by the fin volume. The CFD and experiments for Tube 1 and 2 show an order of magnitude improvement relative to baseline tubes A-C when compared by $TPF^*$.

The increase in performance of Tubes 1 and 2 relative to the CFD is attributed to the decrease in pin diameter and length arising from limitations in the additive manufacturing process as well as surface roughness.

*Table 5: Experimental data set.*

| | **11** | **14** | **21** | **24** | **ATE A** | **ATE B** | **ATE C** | **CFD** |
|---|---|---|---|---|---|---|---|---|
| **Type** | Exp | Exp | Exp | Exp | Exp | Exp | Exp | CFD |
| $\boldsymbol{Re}$ | 1.223E+05 | 1.218E+05 | 1.226E+05 | 1.212E+05 | 1.200E+05 | 1.200E+05 | 1.200E+05 | 1.203E+05 |
| $\boldsymbol{Pr}$ | 1.007 | 1.086 | 1.009 | 1.086 | 1 | 1 | 1 | 1.130 |
| $\boldsymbol{Nu}$ | 544.13 | 549.19 | 502.69 | 523.80 | 581.99 | 462.39 | 446.84 | 320.17 |
| $\boldsymbol{u_{Nu}}$ | 24.49 | 28.25 | 22.60 | 29.65 | 87.30 | 69.36 | 67.03 | - |
| $\boldsymbol{f}$ | 0.133 | 0.132 | 0.127 | 0.125 | 0.474 | 0.446 | 1.065 | 0.052 |
| $\boldsymbol{u_f}$ | 0.017 | 0.017 | 0.016 | 0.016 | 0.024 | 0.022 | 0.053 | - |
| $\boldsymbol{\eta}$ | 0.975 | 0.971 | 0.970 | 0.963 | 0.897 | 0.854 | 0.592 | 0.972 |
| $\boldsymbol{Nu_0}$ | 263.06 | 274.35 | 263.77 | 273.29 | 257.90 | 257.90 | 257.90 | 278.06 |
| $\boldsymbol{f_0}$ | 0.017 | 0.017 | 0.017 | 0.017 | 0.017 | 0.017 | 0.017 | 0.017 |
| $\boldsymbol{TPF}$ | 1.048 | 1.018 | 0.980 | 0.991 | 0.749 | 0.607 | 0.439 | 0.798 |
| $\boldsymbol{u_{TPF}}$ | 0.065 | 0.068 | 0.061 | 0.070 | 0.113 | 0.092 | 0.066 | - |
| $\boldsymbol{V/V_0}$ | 0.973 | 1.022 | 1.070 | 1.064 | 1.129 | 1.607 | 3.507 | 1.370 |
| $\boldsymbol{u_{V/V_0}}$ | 0.089 | 0.101 | 0.096 | 0.110 | 0.255 | 0.364 | 0.793 | - |
| $\boldsymbol{TPF^*}$ | 1.030 | 1.000 | 0.484 | 0.490 | 0.008 | 0.009 | 0.007 | 0.788 |
| $\boldsymbol{u_{TPF^*}}$ | 0.064 | 0.067 | 0.030 | 0.035 | 0.001 | 0.001 | 0.001 | - |

It is important to compare the performance of the optimization-inspired pin array to other architectures to determine the value of this technology.

The recuperator specific mass, $m_{sp,r} = m_r/Q$, and pressure drop, $\Delta P_r$, were determined experimentally from the midpoint ($Re = 1.22 \times x10^5$) of each Wilson plot analysis.

$m_{sp,r}$ is plotted as a function of $\Delta P_r$ in Figure 18. Results at the present conditions for the helical pin fin tube are reported, as well as, results for plate pin fin, printed circuit heat exchangers (PCHE), and shell and tube (including one micro-shell-and-tube scenario, point with lowest specific mass)[22]. The average uncertainty, calculated using the Kline and McClintock approach, in $m_{sp,r}$ and $\Delta P_r$, is 0.0085 kPa and 0.048 kg/kW, respectively. These uncertainties are smaller than the error markers and are not shown.

The helical pin fin results are clustered at low $\Delta P_r$. To compare to the PCHE performance, a power law regression is performed on the PCHE model data, and the best fit equation is $m_{sp,r} = 1.6478\Delta P_r^{-0.347}$. The tested helical pin fin heat exchanger has 21.6% lower $m_{sp,r}$ at test condition 1 and 42.7% lower $m_{sp,r}$ at test condition 4. This data suggests that the helical pin fin design is competitive with the PCHE technology.

A direct comparison between the helical pin fin and plate pin fin technologies is not possible since data for plate pin fin designs are not available for $\Delta P_r$ < 10 kPa. However, one plate pin fin design, $\Delta P_r = 14$

kPa, achieves a small $m_{sp,r}$ suggesting that the plate pin fin technology may be competitive with helical pin fin technology for $\Delta P_r = 1$ to 10 kPa class heat exchangers.

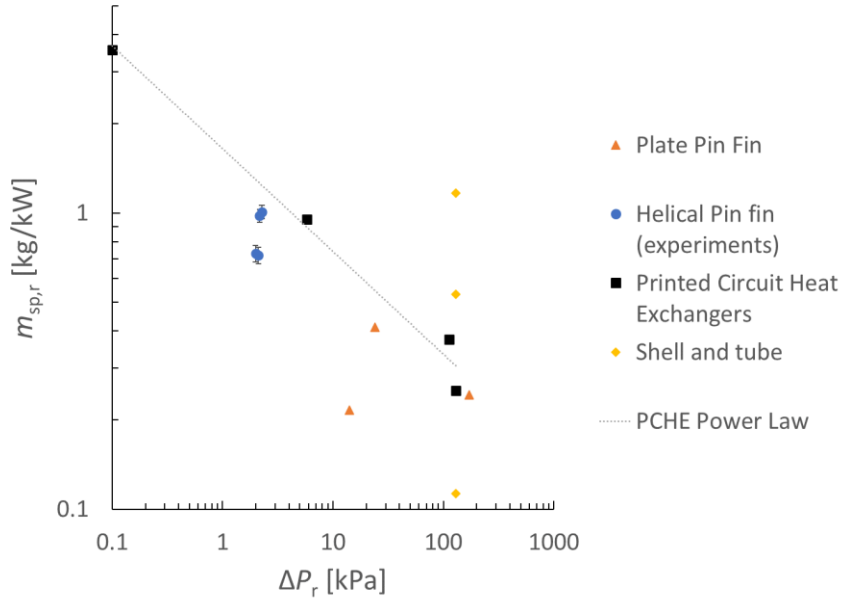


*Figure 18: $m_{sp,r}$ is plotted as a function of $\Delta P_r$ for the present optimized, helical pin fin design and several competing technologies as reported previously (Robey et al., 2022). The 95% confidence interval in the helical pin fin results is less than the marker size.*

## 5. Conclusions

Experiments were conducted to evaluate the heat transfer performance of a helical pin array design inspired by direct single objective optimization. The design showed potential to enhance heat transfer on the tube side of an additively manufactured $sCO_2$ heat exchanger. Two designs were manufactured. The first was the optimization-inspired design and the second was identical except the pin diameter was increased by a factor of two as a precaution if the features on the first tube could not be printed. The designs were CT scanned to study the build accuracy. Two test conditions were considered at temperatures and pressures typical of a $sCO_2$ Brayton Cycle recuperator. The following conclusions may be made concerning the results:

- The "as-printed" features of the first and second tube designs deviated from the design parameters due to additive manufacturing feature size limitations.
- Experimental testing indicated that the optimization-inspired design yielded a 14% improvement in Nusselt number, at equal friction factor, relative to the best performing CFD candidate design.
- The tube design with the larger diameter pin fins had equal performance, within a 95% confidence interval, as the design with smaller diameter fins.
- Fin array efficiency approached 1 due to the small fin size for both designs.
- The tested optimal design had a friction factor four times smaller than those measured experimentally in baseline pinned tube designs at equal Nusselt number.
- The $V/V_0$ thermal performance factor is recommended for quantifying internal cooling performance in this scenario, where it is desirable to reduce heat exchanger tube material.

- On a kg/kW basis, the helical pin fin technology is competitive with printed circuit heat exchangers in a comparable pressure drop specification.

## Acknowledgements

This work was supported by the NETL Supercritical Carbon Dioxide Field Work Proposal awarded by the U.S. DOE Office of Fossil Energy and Carbon Management (FECM). The authors would like to acknowledge the support of former Program Technology Manager, Richard Dennis. James Black developed the concept and the authors for are grateful for his guidance and support. The authors are grateful to Dustin Crandall and his team in NETL Geomaterials Characterization for computed tomography (CT) scans of the test articles. Furthermore, Site Operations Support personnel including Dennis Lynch, Jeff Riley, and Richard Eddy, made critical contributions to the experimental effort. We would like to thank Arnab Roy and Justin Weber for helpful discussions and comments.

## CRediT

**Matthew Searle**: Methodology, Investigation, Formal analysis, Writing – Original Draft, Writing - Review and Editing, **Sridharan Ramesh**: Methodology, Investigation, Formal analysis, **Douglas Straub:** Conceptualization, Project administration, Funding acquisition

## Disclaimer



## References

[1] Brun, K., Friedman, P., & Dennis, R. (2017). Fundamentals and Applications of Supercritical Carbon Dioxide (sCO2) Based Power Cycles. Woodhead Publishing.

[2] Marion, J., Lariviere, B., McClung, A., & Mortzheim, J. (2021). The STEP 10 MWe sCO2pilot demonstration status update. Proceedings of the ASME Turbo Expo, GT2023-58981. https://doi.org/10.1115/GT2021-58981

[3] Searle, M., Black, J., Straub, D., Robey, E., Yip, J., Ramesh, S., Roy, A., Sabau, A. S., & Mollot, D. (2020). Heat transfer coefficients of additively manufactured tubes with internal pin fins for supercritical carbon dioxide cycle recuperators. Applied Thermal Engineering, 181, 116030. https://doi.org/https://doi.org/10.1016/j.applthermaleng.2020.116030

[4] Roy, A., Searle, M., Ramesh, S., & Straub, D. (2022). Investigation of Gas Turbine Internal Cooling using Supercritical CO2 – Effect of surface roughness and channel aspect ratio. Journal of Engineering for Gas Turbines and Power, 144(November 2022), 1–15. https://doi.org/10.1115/1.4055497

[5] Searle, M., Roy, A., Black, J., Straub, D., & Ramesh, S. (2021). Investigating Gas Turbine Internal Cooling Using Supercritical CO2 at Higher Reynolds Numbers for Direct Fired Cycle Applications. Journal of Turbomachinery, 144(1), 1–15. https://doi.org/10.1115/1.4052138

[6] Richardson, J., Wardell, J., Fernandez, E., & Kapat, J., (2023) Experimental and Computational Heat Transfer Study of sCO2 Single-jet Impingement, Proceeding of ASME Turbo Expo 2023, June 26-30, 2023, Boston, Massachusetts, GT2023-102544.

[7] Wardell, R. J., Richardson, J., Otto, M., Smith, M., Fernandez, E., & Kapat, J., (2023) An Experimental Investigation of Heat Transfer for Supercritical Carbon Dioxide Cooling in a Staggered Pin Fin Array, Proceeding of ASME Turbo Expo 2023, June 26-30, 2023, Boston, Massachusetts, GT2023-103263.

[8] Jiang, Y., Liese, E., Zitney, S. E., & Bhattacharyya, D. (2018a). Design and dynamic modeling of printed circuit heat exchangers for supercritical carbon dioxide Brayton power cycles. Applied Energy, 231, 1019–1032.

[9] Cox, T. L., & Fourspring, P. M. (2014). Comparison measured and analytical performence of shell-and-tube heat exchanges cooling and heating supercritical carbon dioxide. The 4th International Symposium - Supercritical CO2 Power Cycles, 1–9.

[10, Fourspring 2018] Fourspring, P. M., Nehrbauer, J. P., & Jia, Z. (2018). Thermal-hydraulic testing of a compact, diffusion bonded heat exchanger for a supercritical CO2 Brayton power cycle. The 6th International Symposium - Supercritical CO2 Power Cycles, 1–7.

[11] Portnoff, M., Vahdat. V., & Chordia, L., (2022) "Design, Fabrication, and Testing of Novel Compact Recuperators for the Supercritical Carbon Dioxide Brayton Power Cycle," The 7th International Supercritical CO2 Power Cycles Symposium, February 21—24, 2022, San Antonio, Texas. Paper # 175.

[12, Pidaparti 2018] Pidaparti, S. R., Ranjan, D., & Anderson, M. (2018). Thermal-hydraulic performance of discontinuous fin heat exchanger geometries using supercritical CO2 as the working fluid. The 6th International Symposium - Supercritical CO2 Power Cycles.

[13, Naderi 2018] Naderi, C., Rasouli, E., & Narayanan, V. (2018). Design and performance characterization of a micro-pin fin sCO2 recuperator. The 6th International Symposium - Supercritical CO2 Power Cycles.

[14] Jiang, Y., Liese, E., Zitney, S. E., & Bhattacharyya, D. (2018b). Optimal design of microtube recuperators for an indirect supercritical carbon dioxide recompression closed Brayton cycle. Applied Energy, 216, 634–648. https://doi.org/https://doi.org/10.1016/j.apenergy.2018.02.082

[15] Chordia, L. (2017). High Temperature Heat Exchanger Design and Fabrication for Systems with Large Pressure Differentials, Thar Energy, LLC, Final report, DOE Project: DE-FE00024012.

[16] Kelly, J., Arft, D., Weisse, S., & Baggett, A. (2016). High Effectiveness, Compact, High Pressure and Low Cost Recuperator for Super-Critical CO 2 Power Cycles. The 5th International Symposium - Supercritical CO2 Power Cycles.

[17] Sabau, A. S., Bejan, A., Brownell, D., Gluesenkamp, K., Murphy, B., List, F., Carver, K., Schaich, C. R., & Klett, J. W. (2020). Design, additive manufacturing, and performance of heat exchanger with a novel flow-path architecture. Applied Thermal Engineering, 180(July), 115775. https://doi.org/10.1016/j.applthermaleng.2020.115775

[18] Robey, E. H., Ramesh, S., Sabau, A. S., Abdoli, A., Black, J. B., Straub, D. L., Yip, M. J., Robey, E. H., Sabau, A. S., Abdoli, A., Black, J. B., Straub, D. L., Yip, M. J., Ramesh, S., Sabau, A. S., Abdoli, A., Black, J. B., Straub, D. L., Yip, J., & Yip, M. J. (2022). Design Optimization of an Additively Manufactured Prototype Recuperator for Supercritical CO2 Power Cycles. Energy, 251, 12. https://doi.org/https://doi.org/10.1016/j.energy.2022.123961

[19] ANSYS Fluent Theory Guide. 2022 R1.

[20] Incroprera, F. P., Dewitt, D. P., Bergman, T. L., & Lavine, A. S. (2007), *Fundamentals of Heat and Mass Transfer,* 6th Edition, John Wiley, and Sons.

[21] ANSYS, Inc. (2023), *DesignXplorer User's Guide,* 2023 R1, Available at https://ansyshelp.ansys.com/account/secured?returnurl=/Views/Secured/corp/v231/en/wb_dx/dxbook.html

[22] Black, J., Straub, D., Robey, E. H., Yip, M. J., Ramesh, S., Roy, A., & Searle, M. (2020). Measurement of Convective Heat Transfer Coefficients With Supercritical Co2 Using the Wilson-Plot Technique. Journal of Energy Resources Technology, 142(July), 1–10. https://doi.org/10.1115/1.4046700

[23] Kline, S., & McClintock, F. (1953). Describing uncertainties in single-sample experiments. In Mechanical engineering.

[24] White, C., Shelton, W., & Dennis, R. (2014). An Assessment of Supercritical CO2 Power Cycles Integrated with Generic Heat Sources. The 4th International Symposium-Supercritical CO2 Power Cycles.

[25] Dostal, V., Driscoll, M. J., & Hejzlar, P. (2004). A supercritical carbon dioxide cycle for next generation nuclear reactors. Massachusetts Institute of Technology, Department of Nuclear Engineering.

[26] Webb, R. L. (1981). Performance evaluation criteria for use of enhanced heat transfer surfaces in heat exchanger design. International Journal of Heat and Mass Transfer, 24(4), 715–726. https://doi.org/https://doi.org/10.1016/0017-9310(81)90015-6